Paper accepted in "International Journal of Machine Tools and Manufacture" (March 2021)
GOLD open access

In-depth microscopic characterisation of the weld faying interface revealing stress-induced metallurgical transformations during friction stir spot welding

Danka Labus Zlatanovic[a,b+], Sebastian Balos[a], Jean Pierre Bergmann[b], Stefan Rasche[b], Janez Zavašnik[c], Vishal Panchal[d], Leposava Sidjanin[a] and Saurav Goel[e,f,g*]

[a]Department of Production Engineering, Faculty of Technical Science, University of Novi Sad, Novi Sad, Serbia
[b]Department of Production Technology, Technische Universität Ilmenau, Ilmenau, Germany
[c]Jožef Stefan Institute, Jamova cesta 39, SI-1000 Ljubljana, Slovenia
[d]Bruker UK Ltd, Banner Lane, Coventry, CV4 9GH, UK
[e]School of Engineering, London South Bank University, London, SE10AA, UK
[f] School of Aerospace, Transport and Manufacturing, Cranfield University, Cranfield, MK43 0AL, UK
[g]Department of Mechanical Engineering, Shiv Nadar University, Gautam Budh Nagar, 201314, India

Corresponding author Email ID: [*]GoeLs@Lsbu.ac.uk and [+]danlabus@uns.ac.rs

Abstract

Friction stir spot welding (FSSW) is a solid-state welding process, wherein the properties of a weld joint are influenced by the state of friction and localised thermodynamic conditions at the tool-workpiece interface. An issue well-known about FSSW joints is their lack of reliability since they abruptly delaminate at the weld-faying interface (WFI). This study explores the origins of the delamination of multiple lap welded aluminium alloy (AA 5754-H111) sheets joined by FSSW at different rotational speeds typically used in industry. Experimental techniques such as the small punch test (SPT), Vickers hardness test, Scanning Electron Microscopy (SEM), Scanning Acoustic Microscope (SAM), Transmission Electron Microscopy (TEM), Energy-dispersive X-ray spectroscopy (EDX) and Frequency-Modulated Kelvin Probe Force Microscopy (FM-KPFM) were employed. The experimental results revealed that a complex interplay of stress-assisted metallurgical transformations at the intersection of WFI and the recrystallised stir zone (RSZ) can trigger dynamic precipitation leading to the formation of Al_3Mg_2 intermetallic phase, while metallic oxides and nanopits remain entrapped in the WFI. These metallurgical transformations surrounded by pits, precipitates and oxides induces process instability which in turn paves way for fast fracture to become responsible for delamination.

Keywords: Friction stir spot welding; delamination; weld faying interface; small punch test, dynamic precipitation

Abbreviations:

BF	**Bright field**
BLs	**Bonding ligaments**
DB	**Diffusion bonding**
DRZ	**Diffusion resistant zone**
EDX	**Energy-dispersive X-ray spectroscopy**
FEA	**Finite Element Analysis**
FIB	**Focused ion beam**
FM-KPFM	**Frequency-modulated Kelvin probe force microscopy**
FGRZ	**Frustrated granular refined zone**
FSSW	**Friction stir spot welding**
HAADF	**High-angle annular dark-field**
rpm	**Revolutions per minute**
RSZ	**Recrystallized stir zone**
PLT-FSSW	**Friction stir spot welding with pin-less tool**
SAM	**Scanning acoustic microscope**
SEM	**Scanning electron microscopy**
SP	**Surface potential**
SPT	**Small punch test**
STEM	**Scanning transmission electron microscopy**
TEM	**Transmission electron microscopy**
WFI	**Weld faying interface**

Nomenclature:

$\sigma_{n\,(t)}$	**Axial stress**
$\tau(t)$	**Shear stress**
Rp	**Radius of the punch**
Ds	**Diameter of the specimen**
h	**Thickness of the specimen**
r_d	**Radius of the die**
r_t	**Contact radius**
d_d	**Internal diameter of the die**
Φ_{sample}	**Work function of the sample**
Φ_{probe}	**Work function of the probe**
E	**Charge of an electron**
ΔV_{CPD}	**Contact potential difference between the probe and the sample**

1. Introduction

Weight reduction has become a key driver in the transport sector for improving fuel efficiency and thereby to achieve sustainability. Generally, a weight reduction of about 10% of an automobile can reduce its specific fuel consumption by 3 to 7 % and CO_2 emissions by 9 g/km [1]. One of the recent trends in the automotive industry has been replacing copper alloys with aluminium alloys due to their lower density while achieving the same electrical conductivity. Consequently, friction stir spot welding (FSSW) is emerging as a promising technology for solid-state joining of weld battery components, strand-terminal connectors and terminals. However, the joining of aluminium alloys, particularly with solid-state welding techniques is a challenging task due to a tenacious and undesirable chemically stable aluminium oxide layer that forms on the surface of the sheets due to the surface oxidation [2] before the welding. **Fig. 1** schematically illustrates the current understanding on this topic elucidating the adverse role that an oxide layer can play in disturbing the homogeneity of the bonding mechanism of aluminium sheets during a solid-state pin-less tool friction stir spot welding (PLT-FSSW) process.

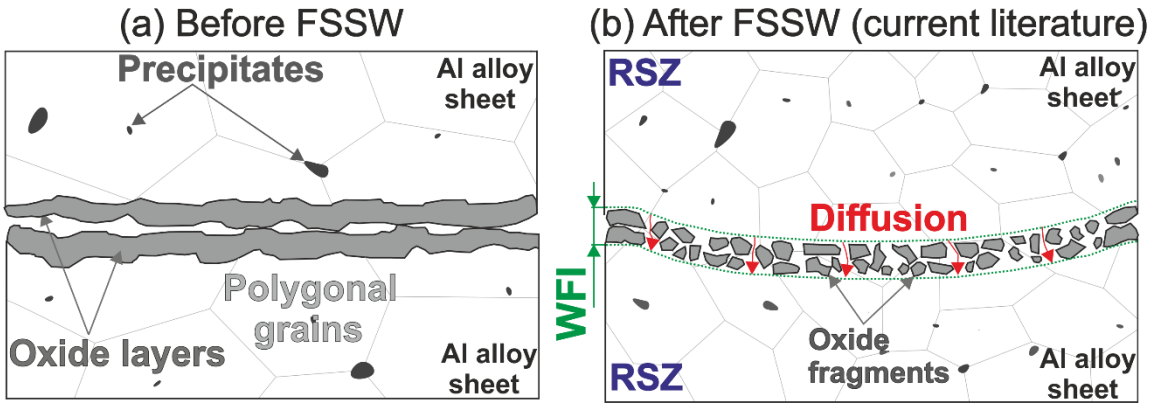

Fig. 1: Extant literature illustrating the role of surface oxidation during friction stir spot welding **(a)** Interfacial thin oxide layer at the interface of the sheets before the welding and **(b)** interrupted diffusion bonding due to the smaller oxide fragments (WFI-weld faying interface; RSZ- recrystallised stir zone) being harder and brittle than the pristine workpiece material

A conventional friction stir spot welding employs the tool with a pin which helps to stir the material in the weld zone homogenously and a careful optimisation of the process parameters [3] and tool geometry [4] has led to very good quality of weld joints so the problem posed by the oxide layer in this case is not as severe as it is when using a pinless tool.

Efforts have also been made to deploy numerical analysis studies to gain good insights about the FSSW process, particularly about the nature of material flow [5], however, finite element analysis (FEA) by its very nature can not reveal the microstructural changes occurring at the sub-micron scale. More recently, researchers from all over the globe have put collective efforts to explore the physics of material removal, chipping and plasticisation effects occurring during friction stir welding processes. This includes using a myriad of modelling techniques ranging from process simulations by calibrating the model with experimental parameters [6], computations fluid dynamics [7], but a genuine problem and an impediment in these prediction models has been to understand the material response at high-strain rates such as that occurring during friction welding. So far researchers have alluded to selection criterion for constitutive laws to study friction stir welding [8, 9] and have successfully demonstrated the modelling of

plasticisation effects [10]. An experimental effort such as the one taken in this study complementing these models is very timely.

Moreover, an understanding of the adverse influence that the oxide layer plays in driving the undesirable metallurgical transformations in the weld interface has continued to remain a major knowledge gap to date and elucidating this new knowledge became a key motivation of this work.

During FSSW, the tool induces lateral strain in the sheets, which causes fragmentation of the brittle oxide layer [11]. As these fragments remain entrapped underneath the tool, they impede the homogeneity in the diffusion bonding resulting in non-uniform weld joint quality. Additionally, these sites subsequently become potential sources for the nucleation (hotspots) of fracture and joint failure [5].

In a related technology known as the Diffusion Bonding (DB) process, Shirzadi et al. [2] and Cooper et al. [12] reported the influence of entrapped oxide layers on the weld properties. Sato et al. [11] found that the presence of Al_2O_3 was responsible for the formation of zigzag lines (lazy S) and kissing bond defects near to the root of the weld zone in friction stir welded butt joints of AA 1050. The deformation of the weld faying interface (WFI) during FSSW of multiple sheets differs from other solid-state welding techniques, especially as the WFIs far from the tool (lower sheets) undergo only partial deformation. Due to this, the entrapped oxide and the pits and voids surrounded by entrapped oxides enforce partial bonding. Also, WFI is often referred to as *bonding ligaments* (BLs), and it is considered as one type of defect because fracture during shear tensile tests has been observed to follow the path of growth of the BLs [13].

BLs have been widely studied at the macro and micro scale especially the influence of their length, shape and distribution on the shear strength of the weld joints. Tier et al. [14] studied the influence of rotational speed (in the range of 900 to 1900 rpm) during refill FSSW of AA 5042. They found that shear strength increases with an increase in the length of the bonding ligaments which is caused by a reduction of the rotational speed. Li et al. [15] investigated the influence of rotational speed (varied from 900 to 1700 rpm) on the weld strength during refill FSSW of AA 2A12 aluminium alloy. However, they found that shear strength increases with rotational speed only up to 1300 rpm and then decreases modestly. Overall, these contradictory observations point to the fact that the bonding ligaments are known to play a significant role in governing the weld strength but there is no clarity on their evolution and the influence that they cause on the homogeneity of the joint.

Furthermore, Shirzadi et al. [2] proposed that the problem created by an oxide layer can be remedied by using rougher surfaces as opposed to polished surfaces. However, a rough surface leads to additional micro-deformation of the small protrusions during intense plastic deformation at the mating interfaces, which can cause local grain refinement [16].

The WFI (including bonding ligament) is a complex metallurgically transformed area and gaining a good microscopic understanding of this area is a necessity for making a step advance in FSSW. It is also noteworthy that the intermetallic oxides of aluminium are brittle compared to the pristine aluminium alloy which is ductile. These brittle intermetallic oxides possess the potential of hindering the diffusion bonding process and become the breeding ground for the crack nucleation paving the way for delamination to occur. Addressing these thoughts, this paper develops a deeper understanding of the weld faying interface which was analysed from

weld samples obtained from FSSW at various rotational speeds. The weld samples were subjected to a small punch test and characterised using advanced microscopic techniques such as Transmission Electron Microscopy (TEM), Energy-dispersive X-ray spectroscopy (EDX), Scanning Acoustic Microscope (SAM) and Frequency-modulated Kelvin Probe Force Microscopy (FM-KPFM) to reveal novel insights about the metallurgical phase changes triggered by stresses in the weld zone.

2. Research methodology and experimentation

2.1 Base material

The base material for FSSW (44 mm × 50 mm) was prepared from 0.3 mm thick rolled commercial aluminium alloy AA 5754-H111 sheets. The chemical composition of the workpiece as determined by optical emission spectroscopy (ARL 3580, Applied Research Laboratories, US) is presented in **Table I**.

Table I: Chemical composition of AA 5754 - H111 aluminium alloy

Element	Si	Fe	Cu	Mn	Mg	Cr	Zn	Ti	Al
wt. (%)	0.19	0.24	0.03	0.30	3.10	0.03	0.005	0.014	bal.

2.2 FSSW process

FSSW experiments were carried out on an adapted force-controlled EJOWELD C50R FSSW machine which can reach a maximum rotational speed of 9000 rpm, a maximum axial load of 8 kN and a maximum penetration time of 5 s. Four thin sheets were lap joined with a customised pin-less tool shown in **Fig. 2**. The tool made from H13 (X40CrMoV51) hot-work tool steel used in this study differs from the previous work [17] as the contact radius here was modified to increase the width of the welded zone and thus the weld strength and to reduce the penetration time. As such it should be noted that the tool here has a convex profile which provides a gradually changing pressure while pressing the thin sheets and presents no sharp corners. A flat tool on the other hand, at the sharp corners, will present higher stresses than the fracture stress of the sheets and will therefore tear the sheets apart. These results with evidence are comprehensively discussed in the previous publication and those details are not repeated here for brevity [17, 18]. The experimental parameters used to perform FSSW in this study are presented in **Table II**.

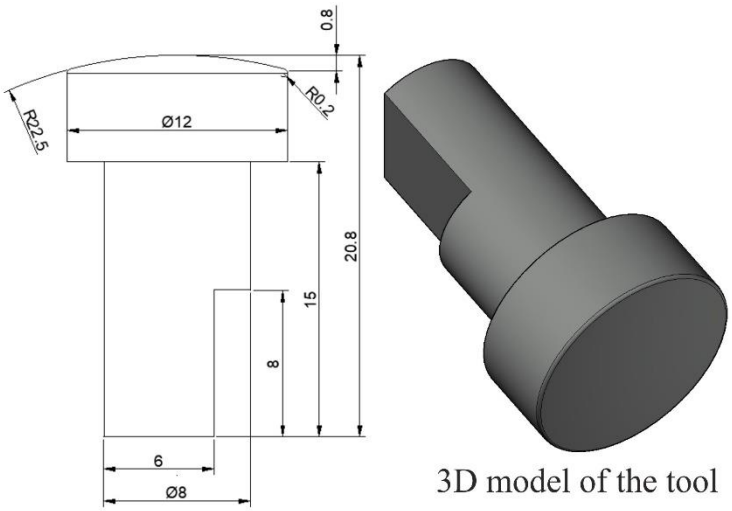

Fig. 2: Details of pinless tool geometry used for the friction stir spot welding.

Table II: Friction stir spot welding parameters used in this work

Sample	Rotational speed (rpm)	Axial load (kN)	Penetration depth (mm)	Penetration time (s)
S1	1000	4	0.25	1.68±0.07
S2	2000			1.11±0.04
S3	3000			0.98±0.04
S4	4000			0.97±0.04

2.3 Mechanical testing

2.3.1 Microhardness

The tensile strength and yield strength of the aluminium alloy used were tested by using a Hegewald & Peschke Inspect Retrofit universal tensile testing machine. A Struers DuraScan 70 instrument at a load of 0.1 kg was used to obtain the Vickers hardness of the base material. All measurements were repeated three times and the results obtained from the tests with standard deviation are presented in **Table III**. As for the weld surfaces, a microhardness mapping was obtained by indenting an array with a spacing of 0.33 mm between two indents.

Table III: Mechanical properties of the AA 5754 - H111 aluminium alloy used.

Material	Yield strength (MPa)	Tensile strength (MPa)	Vickers microhardness (HV0.1)
AA 5754 – H111	151±0.1	246±0.2	64±2.7

2.3.2 Small Punch Test (SPT)

A small punch test (SPT) is an easy-to-use mechanical test requiring a limited amount of material for testing. Since SPT can accommodate miniaturised specimens, it is suited to investigate the local mechanical properties of heterogenous materials such as spot welds. SPT provides the load-carrying capacity of specimens. Since specimen size during the SPT tests of different samples remains the same, any variation in the failure load during testing between different samples gives a direct relative comparison of the weld strength of the tested samples merely by monitoring the SPT load. For this investigation, a set of welded samples after FSSW was prepared for SPT. This work used the same customized setup developed by Rasche et al. [19] (see **Fig. 3a**). A disc-shaped specimen was centrally positioned in a receiving die and then deformed until failure by an oncoming spherically tipped punch **Fig. 3b**. The SPT setup geometry was modified compared to the geometry recommended by the European "Code of Practice" CWA 15627:2006 [20]. In an SPT test, the outer part of the disc is clamped rigidly between the receiving and counter die (Small Punch Bulge Test) or only positioned loosely between them (Small Punch Drawing Test) to prevent vertical deformation. In this study, an improved experimental setup was used without a screwed counter die so-called "downloader" so the technique used here is comparable to a Small Punch Bending Test.

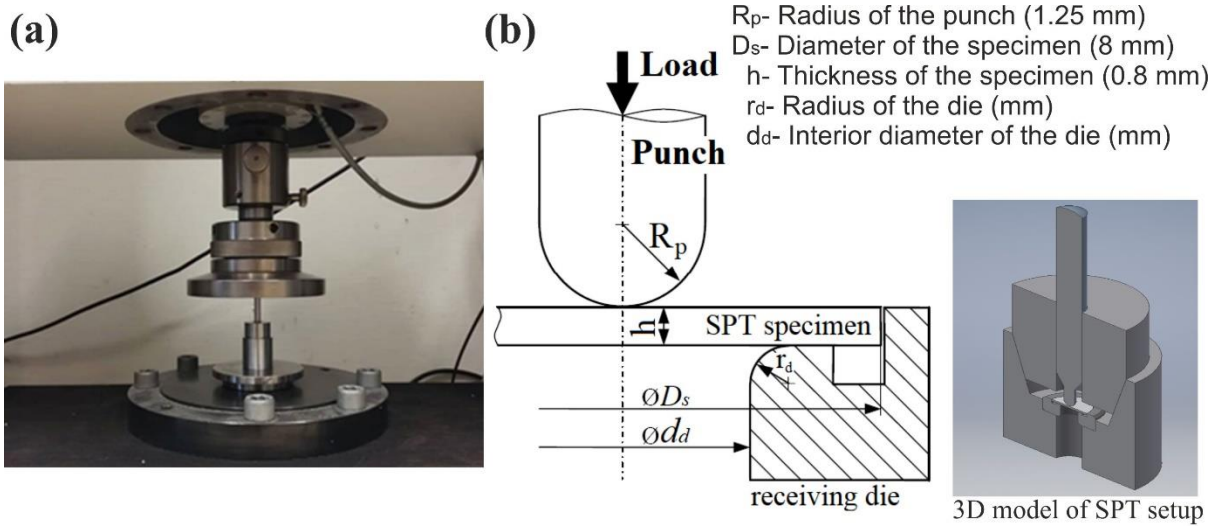

Fig. 3: Detailed small punch test setup: **(a)** Small punch test setup placed on a tensile test machine, **(b)** Customised small punch test setup [19].

The SPT experiments were performed on a Hegewald & Peschke Inspect Retrofit universal testing machine with a maximum load of 20 kN (see **Fig. 3a**) [19]. Based on the experimental observations, a punching speed of 2 mm/min was chosen and specimens were cut to form discs of $8^{-0.005}$ mm diameter. Usually, for small punch tests, the European "Code of Practice" CWA 15627:2006 recommends specimens with a diameter of 8 mm and 0.5 mm thickness. However, in this study, it was essential to consider all three weld interfaces between the four sheets at once, so a specimen thickness of 0.8 mm was considered both for the welded and the base material. The specimens were finely ground with 600, 1200 and 2500 grit abrasive papers to reduce the sheet thickness from ~0.95 mm to $0.8^{\pm 0.01}$ mm as shown in **Fig. 4**. SPT specimens of the base material were cut and prepared from AA 5754-H111 sheet which was 1.2 mm thick. All tests were repeated three times.

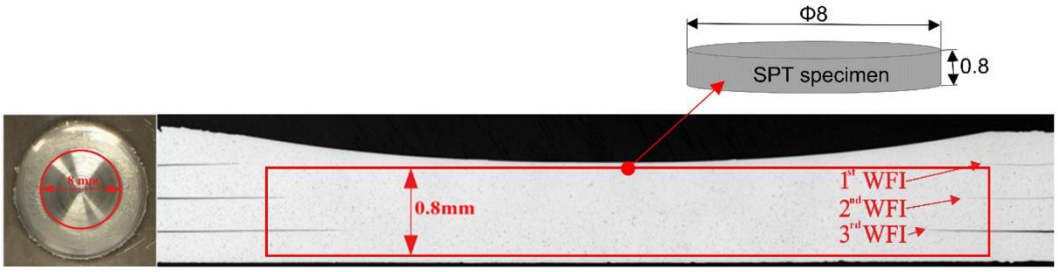

Fig. 1 Small punch test sample showing the sample preparation efforts (WFI: weld faying interface)

2.4 Macrostructure characterisation

Before and after the SPT test, the samples were examined metallographically. All test samples were finely ground with abrasive paper (grit 360 to 2500) and polished with diamond suspension (6 and 3 µm). Colloidal silica of 0.05 µm was used as a final polishing step. The electrolytic etching was performed on a Struers LectroPol-5 device (40 V, 2 min, Barker's regent). The cross-sectional examination was done with a light microscope (Zeiss AxioScope.A1 with AxioCamICc3 with crossed polarized light and sensitive tint was used for etched samples and a Zeiss Axio Vert.A1MAT with AxioCam 105 was used for analysing the polished samples).

The fracture mode of the SPT specimen welded at 1000 rpm was examined with a scanning electron microscope (SEM JSM-6460LV, Jeol Inc.) operating at 15 kV. The WFI of samples welded at 1000 rpm was analysed with a 200 kV transmission electron microscope (TEM, Tecnai Osiris, FEI) additionally equipped with a scanning unit (STEM) including high-angle annular dark-field (HAADF, Fischione Co.) detector and energy dispersive X-ray spectrometer (EDX, Super-X system with 4 Bruker silicon drift detectors, Thermo Fisher Co.). Surface potential (SP) mapping of WFI was carried out using the Frequency-Modulated Kelvin Probe Force Microscope (FM-KPFM, Bruker Dimension Icon XR scanning probe microscope, Bruker Co.) on the same lamella that was prepared for the TEM using focussed ion beam (FIB). Electron-transparent specimens for the TEM and FM-KPFM analysis were prepared by dual-beam FIB-SEM instrument (Crossbeam 550, Zeiss GmbH). **Fig. 5** shows a sample region where the lamella was cut (white square) from the welded specimen (1000 rpm). The grains and precipitate sizes were estimated by using the ImageJ software [21].

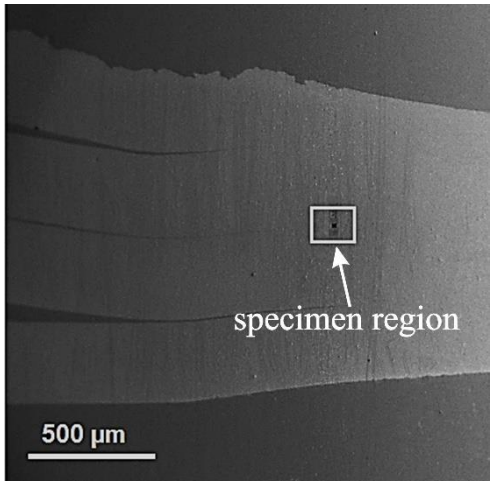

Fig. 5: Cross-sectional secondary-electron scanning electron microscope (SEM) image of the sample welded at 1000 rpm with highlighted area at the interface (square) further analysed by transmission electron microscope (TEM) and frequency-modulated Kelvin probe force microscopy (FM-KPFM).

Additionally, the weld joint topography was assessed using a Scanning Acoustic Microscope (SAM) (PVA TePla made, Westhausen, Germany), equipped with H2 PreAmplifier to understand the nature of the plastic flow at low and high spindle speeds. To perform the SAM, a cross-section of the FSSW sheet sample was immersed in a water tank (deionised water) and an ultrasonic transducer was moved over the sample to collect the data. For this purpose, a transducer PT30-6-12.7 with 20 dB gain, 30 MHz frequency of diameter 6 mm and a focal distance of 12.7 mm was used.

3. Results and Discussions

3.1 Macrostructure and stress analysis of the weld zone

The top views of the weld macrographs and cross-sections of polished and etched samples obtained at rotational speeds ranging from 1000 to 4000 rpm are shown in **Fig. 6**. **Fig. 7** shows the evolution of the axial and shear stresses calculated analytically over the weld duration together with the dynamically changing tool contact radius. The input data used to perform these calculations comes from the instrument in the form of the applied torque and the predefined axial load [12]. Same data was also used to analytically estimate the change in the contact radius using $r(t) = \sqrt{h \cdot (2R - h)}$ (mm) where, *R* is the fixed tool radius (mm) and *r(t)* is the instantaneous contact radius [22] and *h* is the tool plunge depth (mm). Here in these stress calculations, the change in the temperature dependent material behaviour such as softening or hardening was not accounted for. The normal stress $\sigma_n(t) = \frac{F(t)}{r(t)^2 \cdot \pi}$ and the shear stress $\tau(t) = \frac{2 \cdot T(t)}{\pi \cdot r(t)^3}$ were calculated and their ratio (τ/σ_n) was obtained as the kinetic coefficient of friction where, $F(t)$ is the axial load applied during the process (N), $T(t)$ is the measured torque (N·mm). *r(t)* is the time-dependent contact radius (mm) and *R* is the tool radius (mm) [17, 18].

The four outputs obtained at various speeds shown in **Fig. 6** did not reveal any obvious visible defects. The topography of the weld surface obtained at 4000 RPM looked more evenly circular than the one obtained at the speed of 1000 RPM. They were further characterised using SAM which are discussed in the later section.

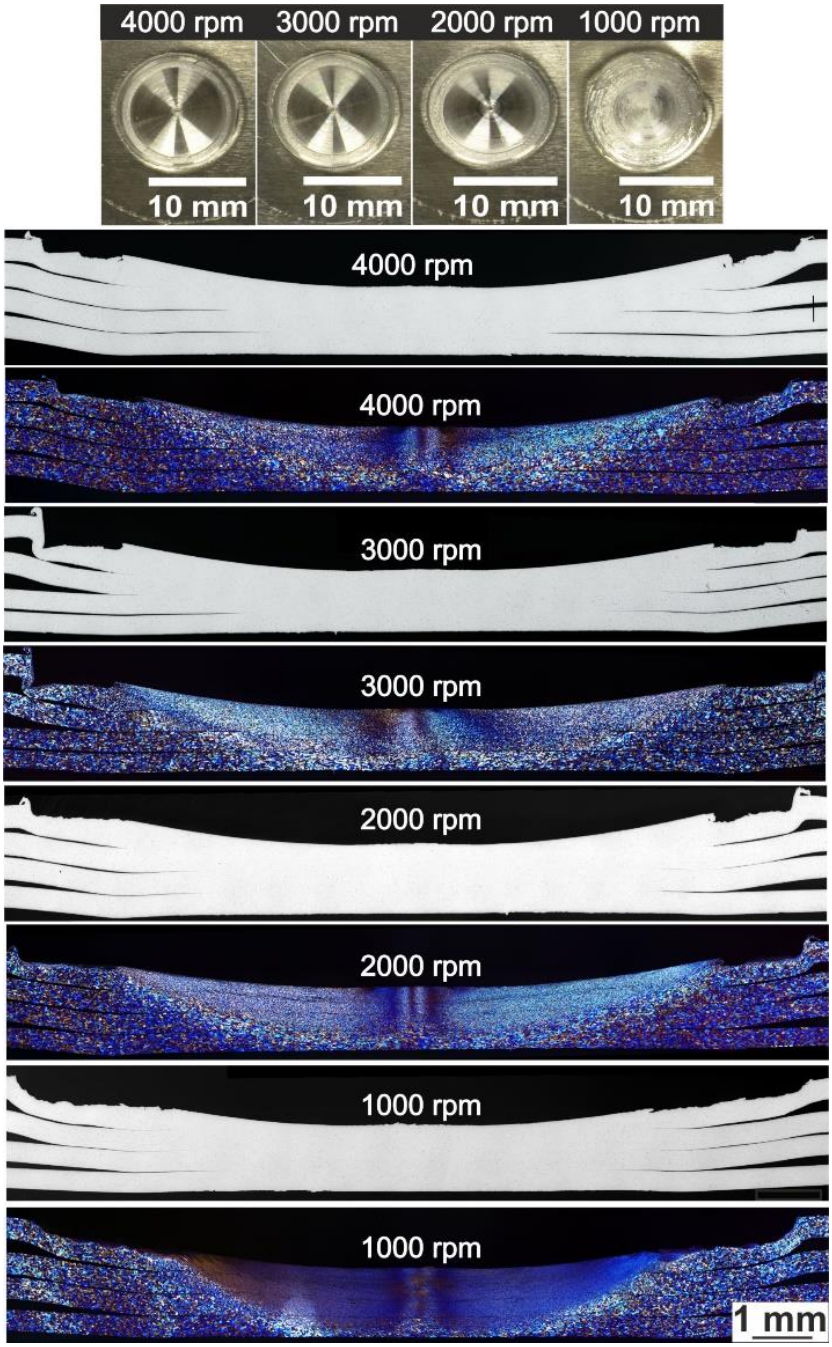

Fig. 6: Top view macrographs, polished and etched cross-section views of the welded joints from 1000 to 4000 rpm

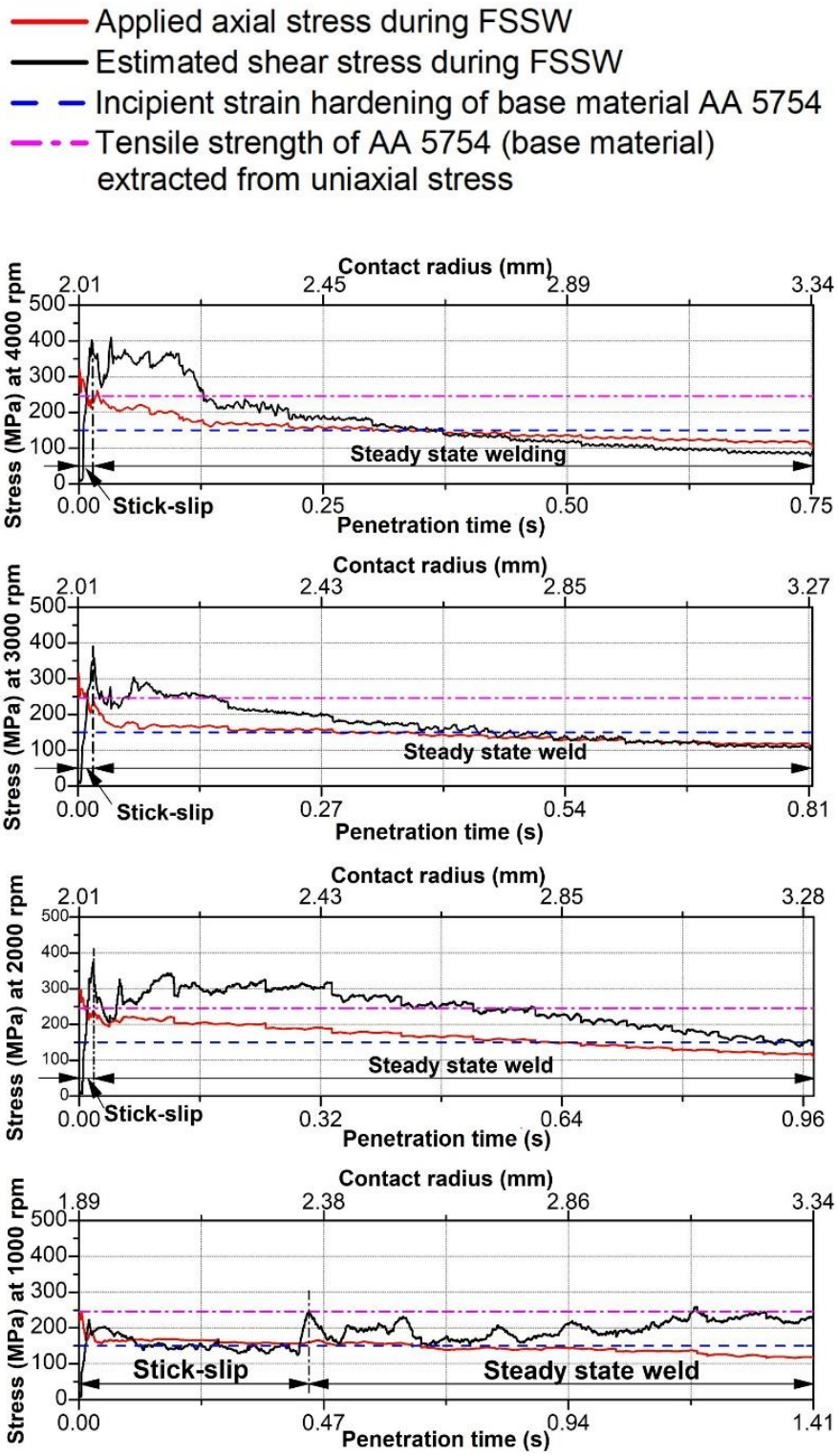

Fig. 7: Evolution of shear and axial stresses over the weld duration referred to as penetration time at spindle speeds from 1000 rpm to 4000 rpm

Some salient aspects of the stress-time curve shown in **Fig. 7** were that the material during the FSSW process passes through two distinct stages namely, the stick-slip zone and steady state welding zone. These zones can distinctly be recognised from the competing stress states i.e., shear stress (by virtue of the rotation of the tool) and the axial pressure applied on the tool. In this *stick-slip* regime, the tool tries to establish stable contact with the workpiece and surface

friction drives the initial stages if the axial stress is higher than shear stress. However, when shear stress exceeds the axial stress, the tool-workpiece achieves a steady-state. Reisgen et al. [23] has described this transition to be the moment where surface friction changes to volumetric friction. In this steady-state, a visco-plastic flow of the material governs the evolution of the stir zone. To maintain the viscous flow of the material, the tool must do sufficient work such that the shear stress remains higher than the thermally dependent yield strength of the material. They have discussed that the dynamic viscosity in AA 5083 alloy during FSSW decreases with the increase of the rotational speed followed by an increase of the temperature and strain rate. According to their observation, in samples welded at higher rotational speeds (2000, 3000 and 4000 rpm), dynamic viscosity decreases. At high rotational speeds, the increasing heat flux causes thermal softening of the material leading to a drop in the value of shear stress. This drop takes the stress level to below the strain hardening limit which was seen during the tensile testing of the material. Also, the higher frictional induced temperature and lower dynamic viscosity during high-speed FSSW cause the dislocations to be absorbed in the grain boundaries during dynamic recovery of the wrought AA 5754 alloy [24].

These observations were in stark contrast to the specific case of low rpm welding such as when the welding was performed at 1000 rpm, where a serrated stress curve (jerky flow) was evident. The shear stress fluctuates (with an increasing trend) between incipient strain hardening of the base material and its ultimate tensile strength (purple and blue line, respectively in **Fig. 7**). As incipient strain hardening and tensile strength for AA 5754 plotted here are strain and temperature dependent, their limits [25], should be considered with caution.

In **Fig. 8**, higher magnification of the sample welded at 1000 rpm is shown. The polished sample in **Fig. 8a** shows no traces of delamination or any type of defects in the weld zone. A uniform weld zone without a visible weld interface can be observed. However, after etching of the sample, bonding ligaments at all three WFI become visible. To understand the influence of WFI on weld properties SPT was performed and analysed in the next section.

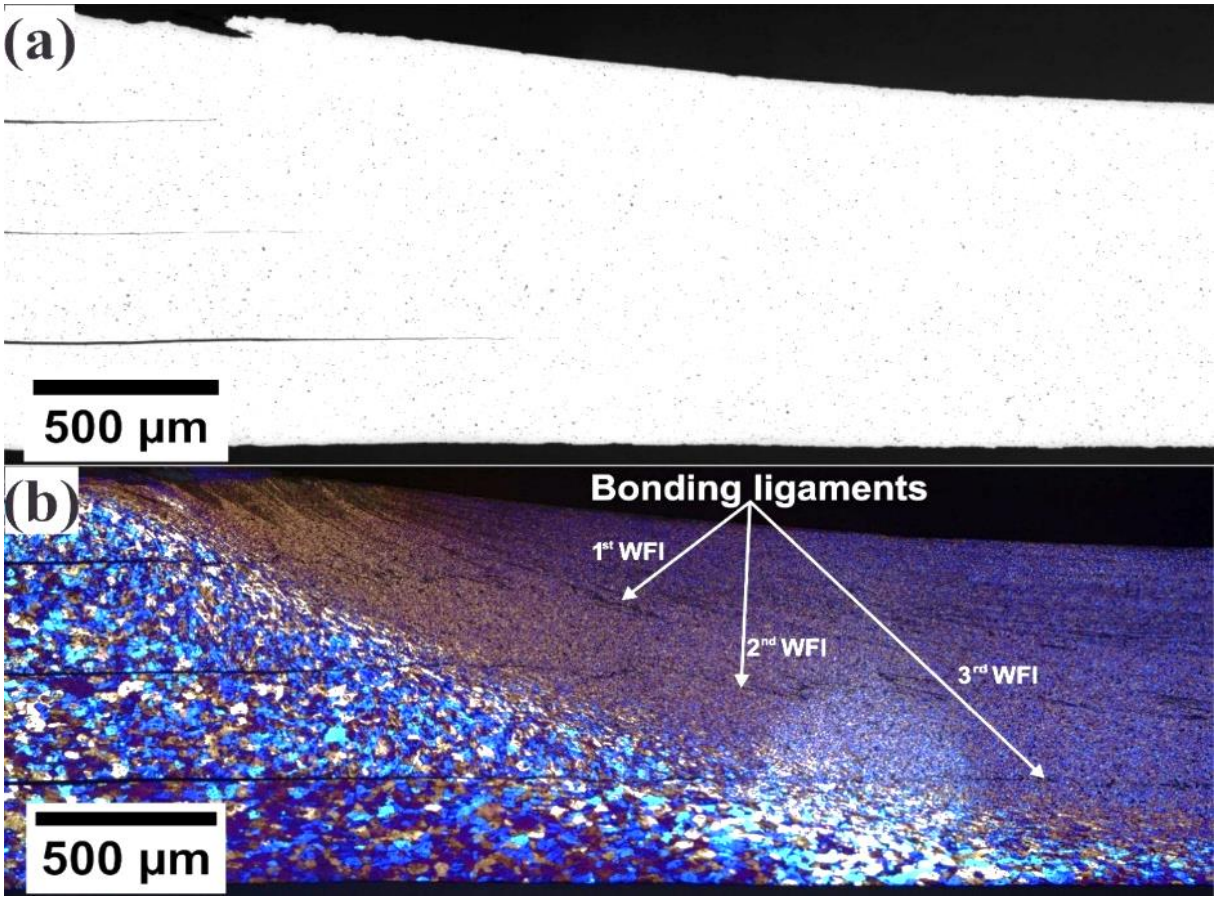

Fig. 8: Optical micrograph of the sample cross-section welded at 1000 rpm: (a) polished cross-section showing no defects in weld zone; (b) etched cross-section showing visible traces of weld faying interface

3.2 Small punch test and microhardness results

Vickers microhardness measurements were done to confirm the results obtained from SPT as well as to gain more localised insights such as strain hardening and thermal softening of the material. During the standard shear tensile test, which is popularly used to test FSSW joints, a fracture path is usually observed at the periphery of the stir zone, or it follows the path of the weld interface [26], therefore no clear image of the local mechanical properties of the stir zone can be described. Therefore, Vickers hardness maps shown in **Fig. 9** were extremely useful in identifying the strain hardening at low rpm and thermal softening occurring at high rpm.

The load-displacement curves comparing the base material and specimens obtained from SPT at different rotational speeds are shown in **Fig. 9a**. Three samples were tested however **Fig. 9a** only shows results for specimens with minimum (most engineering safe) values of rupture load. From **Fig. 9**, two common observations were obtained: (i) weld obtained at 1000 rpm possesses a relatively high microhardness in the stir zone as well as absorbing higher load than the base material to rupture and (ii) the specimens welded at 2000, 3000 and 4000 rpm possess lower hardness in the stir zone and rupture at lower loads. This observation is in line with the previous claims [14] that the increasing rotational speed decreases the weld strength. The results here reaffirmed that thermal softening of the weld zone was responsible for the drop of the weld strength with increasing rotational speed. In line with Vickers hardness maps, **Fig. 10** shows the microstructure granular data of the weld zone obtained from polarized light microscopy.

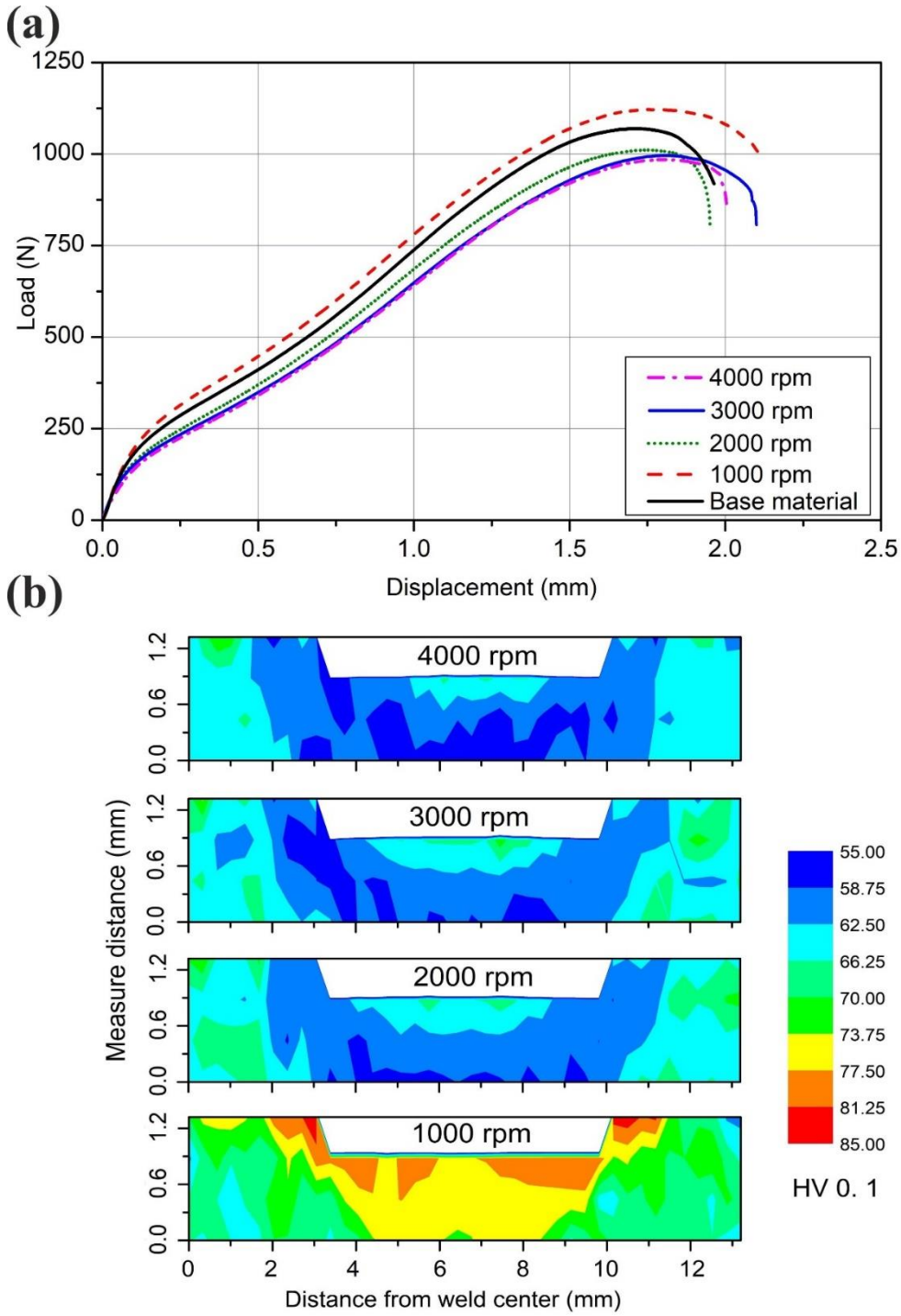

Fig. 9 (a) Small punch test load-displacement curves of base material and weld specimens obtained at rotational speeds between 1000 to 4000 rpm; **(b)** Vickers microhardness maps at the cross-section of samples processed at rotational speeds between 1000 to 4000 rpm

Heating during the FSSW is triggered by the deformation process of material and by friction between the tool and workpiece. Larger rotation speed leads to intense heat release causing thermal softening. In the preceding analysis, all weld samples were seen to have reduced grain size compared to the base material, but the grain size significantly decreases at low rotational speeds. The welded zone consists of three regions namely, the stir zone (SZ), thermomechanical affected zone (TMAZ) and the heat affected zone (HAZ). In this investigation, two clear trends were seen in the granular microstructural data: (i) the grain size increases as we move farther from the stir zone i.e. the grain size in the stir zone was smallest compared to the base material (ii) the grain size

in the stir zone scales linearly with the rotational speed which means lower the speed, lower the grain size or higher the speed, higher the grain size. It seems to suggest that the stir zone processed at low rpm has smaller grain sizes and was harder than the stir zone obtained at 4000 rpm. These observations not only resonate with the Vickers microhardness mapping results but also concord with the stress analysis results discussed previously.

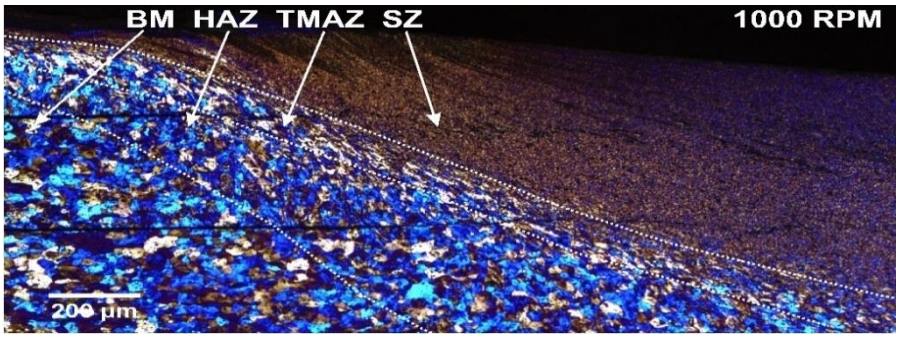

(a) An area in the weld zone showing Base material (BM), Heat affected zone (HAZ), Thermomechanical affected zone (TMAZ) and stir zone (SZ)

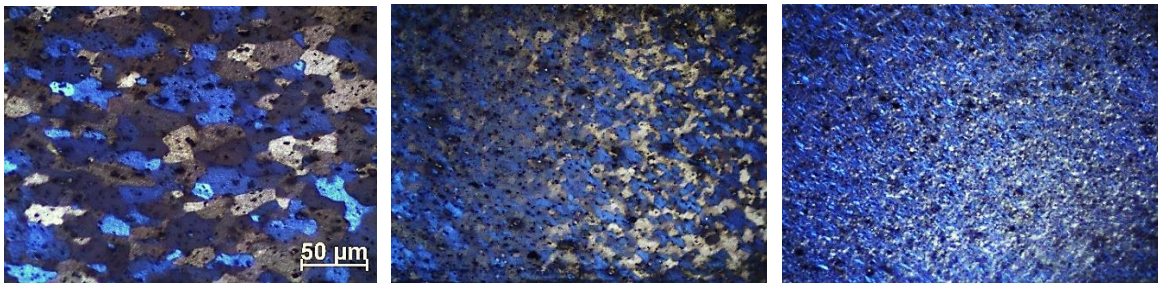

(b) Base material (c) 4000 RPM (d) 1000 RPM

Fig. 10: Grain size distribution obtained in the weld sections shown by using cross-section polarized light microscopy for various conditions of welded samples produced at rotational speeds of 1000 to 4000 RPM

Subsequently, SAM analysis was done on two joint samples obtained at 1000 rpm and 4000 rpm and the SAM results are shown in **Fig. 11** revealing the weld topography from the top with reference to the datum taken as the horizontal bottom surface. The SAM results showed a smooth flow of the material in the stir zone of the material as opposed to chaotic flow conditions at a lower rpm. Moreover, the circularity in the shape of the top sheet after the tool rotation was found to be smoother at higher rpm as opposed to low rpm. This points to the fact that the material flow at a higher rpm was more compliant to the rotational motion of the tool whereas a jerky condition as seen earlier in stress analysis persisted while welding at 1000 rpm. Thus, the extent of pile up of material and the skewed circularity obtained at low (1000) rpm conclusively confirms that the material flow was obstructed by a hardening mechanism.

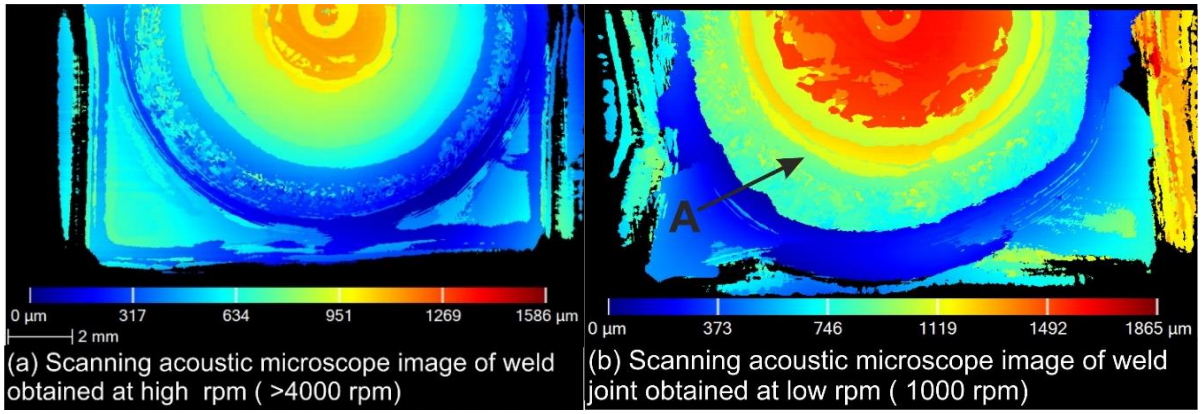

Fig. 11: Comparison of the weld topography obtained from a scanning acoustic microscope (SAM) indicating (a) smooth plastic flow of the material at higher (>4000 rpm) speed thus leading to a true circularity of the shape (less pile-up) and (b) a frustrated hardening mechanism impeding the flow of material at low rpm (pile up indicating strain hardening). Detail A shown in (b) reveals excessive pile-up. Colour bar shows the height map with respect to the reference datum marked in blue colour.

The rupture load and the specimen thinning observed from the SPT tests are presented in **Fig. 12**. A higher deviation in the values of the rupture load for the specimens welded at 1000 rpm is caused by the non-uniform delamination of the specimens. The specimen thinning increases with rotational speed, i.e., specimens after SPT were thicker at 1000 rpm and thinner at 4000 rpm. Such behaviour implies that the specimens subjected to SPT at the same load underwent higher strain when welded at higher rpm than the ones welded at lower rpm.

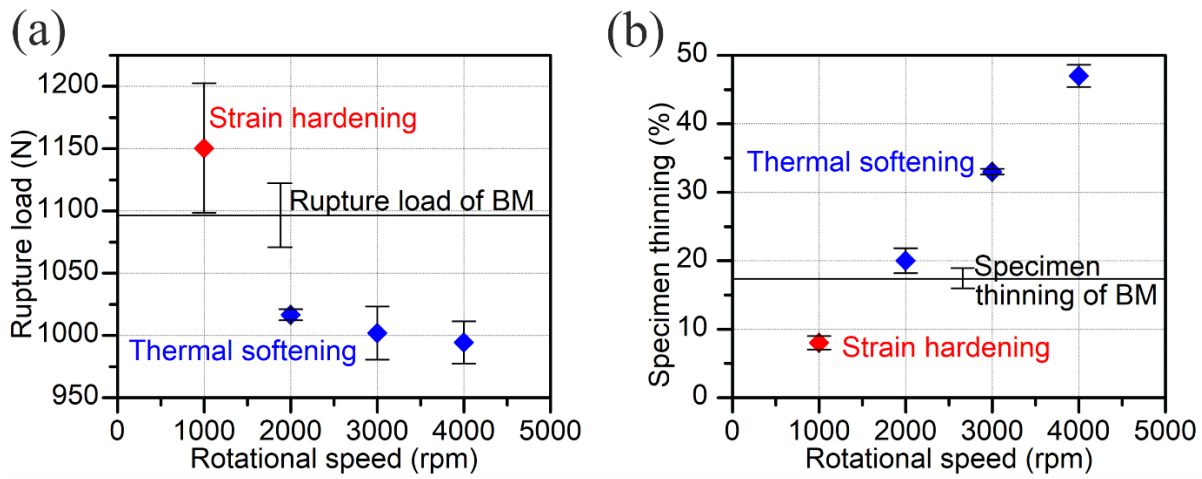

Fig. 12: Rupture load **(a)** and specimen thinning **(b)** as a function of the rotational speed. The error bars show standard deviation.

The macrographs of the specimens after SPT showing graphical evidence of specimen thinning in 2D are shown in **Fig. 13**. In all specimens, radial cracks were visible (highlighted with white arrow) in **Fig. 13.** Further examination of these specimens was done by SEM, as shown in **Fig. 14a**. A crack at approximately 45 degrees to the punch axis was observed, which is representative of a typical SPT fracture [27]. However, in addition to the above observations, the weld specimens obtained at low rotational speeds (1000 and 2000 rpm) showed delamination of the bottom and middle sheets at cross-sections pointed out with red arrows in **Figs. 13 and 14a,b**. The delamination occurred along the WFI marked by the green arrows in **Figs. 13 and 14c,d.**

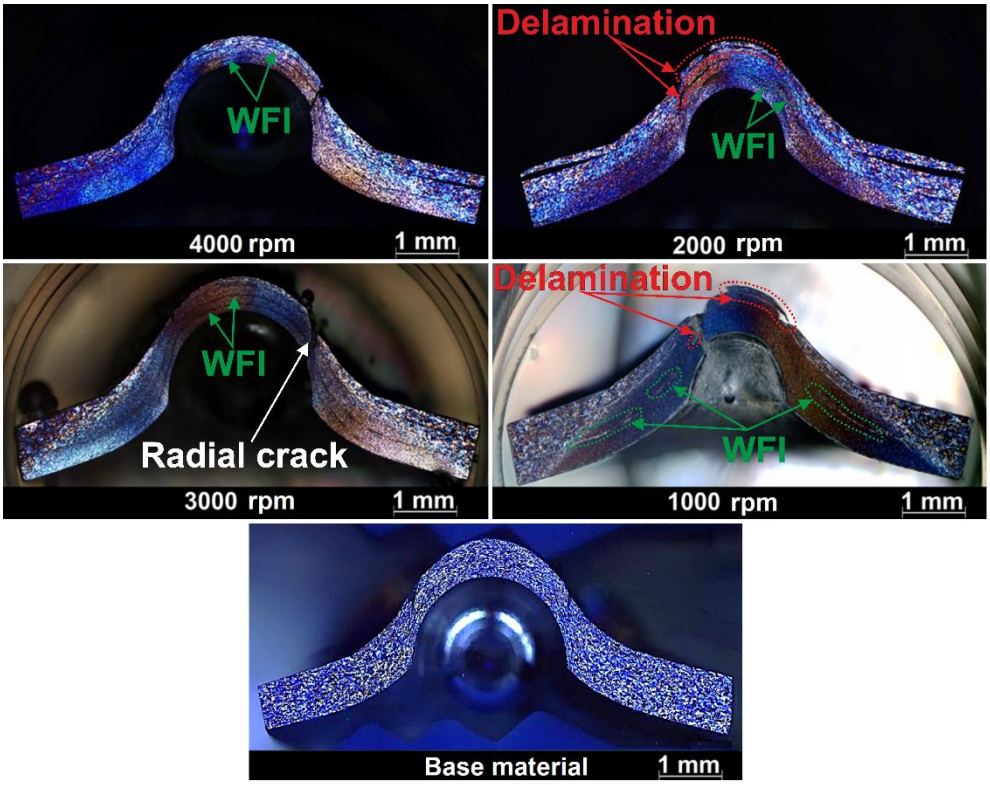

Fig. 13: Macrographs of the specimens after small punch testing prepared from welds produced with rotational speeds in the range of 1000 to 4000 rpm.

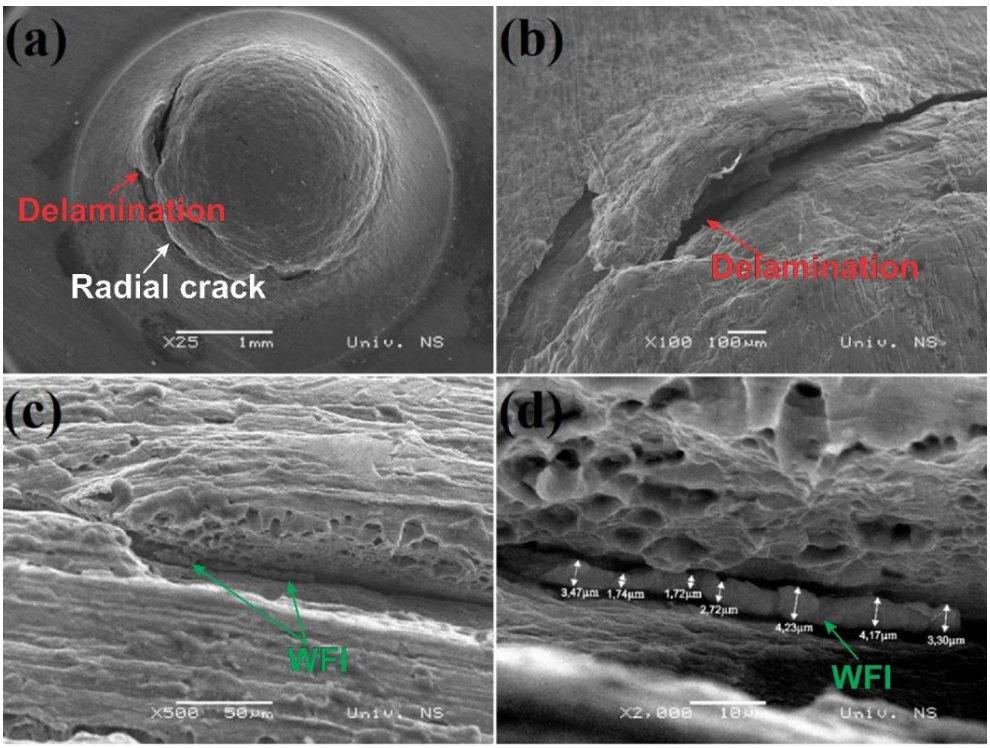

Fig. 14: Scanning electron micrographs of the weld produced at 1000 rpm after small punch test: **(a)** overview micrograph of a ruptured (deformed) sample from a top view; **(b)** enlarged view of the rupture area; **(c)** Scanning electron micrograph of the weld faying interface trapped in rupture; **(d)** close-up of the measured thickness of weld faying interface.

Analysis of the SEM results shown in **Figs. 14b,c** shows that the delamination originated from the WFI. **Fig. 14d** shows the entrapped layer (WFI) in a ruptured void that caused the delamination. It has a different morphology, and its thickness varies between 1.72 and 4.23 µm. For an improved understanding of WFI and its influence on delamination, a TEM analysis was performed.

3.3 Microscopic analysis of weld faying interface using transmission electron microscopy and energy-dispersive X-ray spectroscopy

The STEM bright-field (BF) image of the WFI, including RSZ, is presented in **Fig. 15**. The WFI marked with blue dashed lines in **Fig. 15** was observed to vary in thickness from 1.76 to 2.17 µm, corresponding to the values observed in **Fig. 14d**.

Fig. 15b shows a high-angle annular dark-field (HAADF) micrograph of the WFI. These images show the presence of ultrafine globular precipitates of Al_3Mg_2 in grain boundaries of WFI, originating from dynamic precipitation. A high number of Al_3Mg_2 precipitates with an average size of 0.09 µm were seen at the boundary between RSZ and WFI. The RSZ contains fine recrystallized polygonal grains with an average size of 4.90 µm while WFI contains fibrous grains with an average size of 0.92 µm, as shown in **Table IV**. Polygonal grains in RSZ and fibrous grains in WFI both contain randomly dispersed globular Al_6(FeMn) precipitates which are typical in an AA 5754 alloy [24]. The chemical composition of precipitates was determined by EDX analysis and the spatial distribution of the principal elements was included in **fs. 16a,b and 17a,b.**

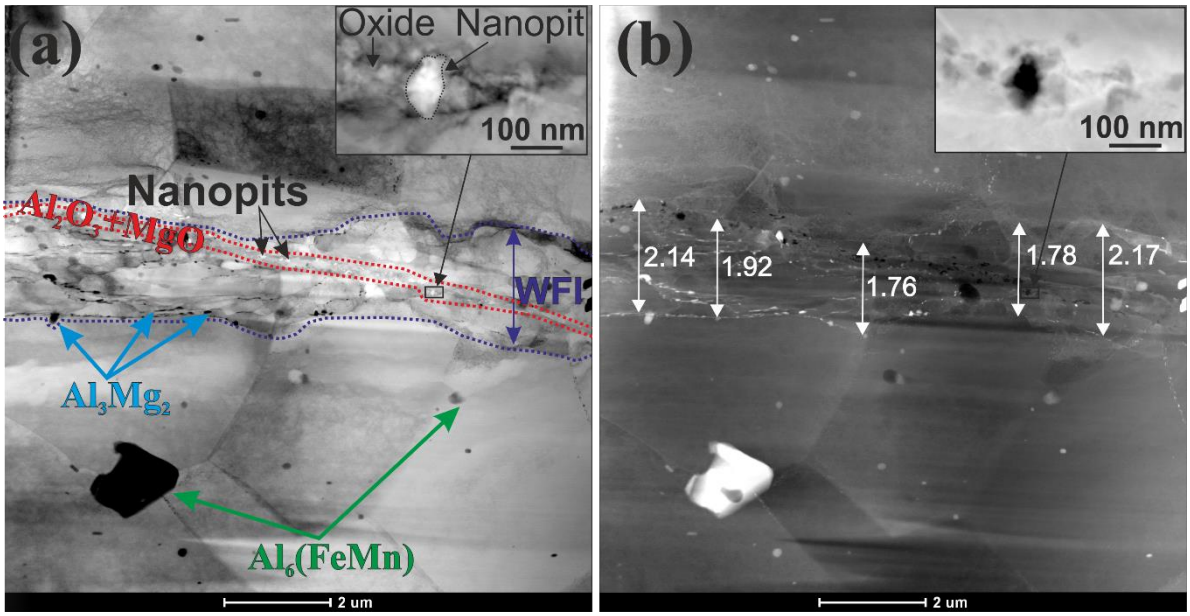

Fig. 15: Scanning transmission electron micrographs of weld faying interface of sample welded at 1000 rpm: **(a)** Bright field scanning transmission electron microscopy (BF-STEM) image; **(b)** High-angle annular dark-field scanning transmission electron microscope (HAADF-STEM) image

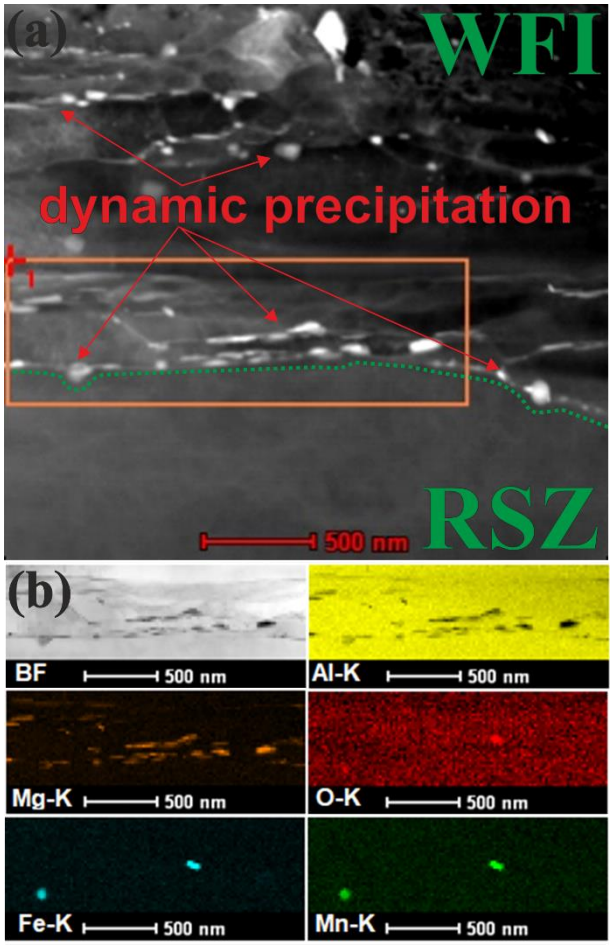

Fig. 16: (a) High-angle annular dark-field scanning transmission electron microscope (HAADF-STEM) image of the boundary between weld faying interface and recrystallised stir zone; **(b)** Bright field scanning transmission electron microscopy image with corresponding energy dispersive X-ray spectroscopy (STEM/EDX) elemental mappings of the area marked in overview (a).

Table IV: Size of the grains and precipitates measured in weld faying interface and recrystallized stir zone.

Area of measurement	Average grain size (μm)	Average precipitates size (μm)
Weld faying interface (WFI)	0.92±0.81	0.09±0.04
Recrystallised stir zone (RSZ)	4.90±0.52	0.15±0.07

At the centre of the WFI, which is the junction of the two sheets, the disturbed oxide layer combined with nano/micro pits were presented with red dashed lines. The aluminium oxide layer acted as a barrier to prevent metal atoms from diffusing from one sheet to form stable bonds with another sheet [28]. During solid-state bonding, usually the oxide layer is about 5 to 10 nm thick Al_2O_3, however, when alloy contains active elements such as Mg, amorphous Al_2O_3 can react with Mg to form crystalline MgO [2] as per the following chemical reaction:

$$Al_2O_3 + 3Mg \rightarrow 3MgO + 2Al \quad (1)$$

Shen et al. [29] found that the welding interface of AA 6061-T4 obtained by the conventional FSSW contained an array of discontinuous oxide particles causing poor welding. Furthermore, Reilly et al. [5] also proposed that the penetration of the tool into the weld zone stretches the weld interface as well as brittle oxide. Thus, diffusion occurs between oxide fragments.

This could be verified from **Fig. 17a**, which shows the area within WFI near the micro pit, surrounded by Al_2O_3 oxide layer (**Fig. 17b**), while in the distal segment, the Al_2O_3 layer changes to MgO (see **Fig. 17c)**. Moreover, the oxide-rich region remains unbonded, filled with micro/nano pits and engulfed by an oxide layer, which acts as a diffusion barrier leaving unbonded spots (pits).

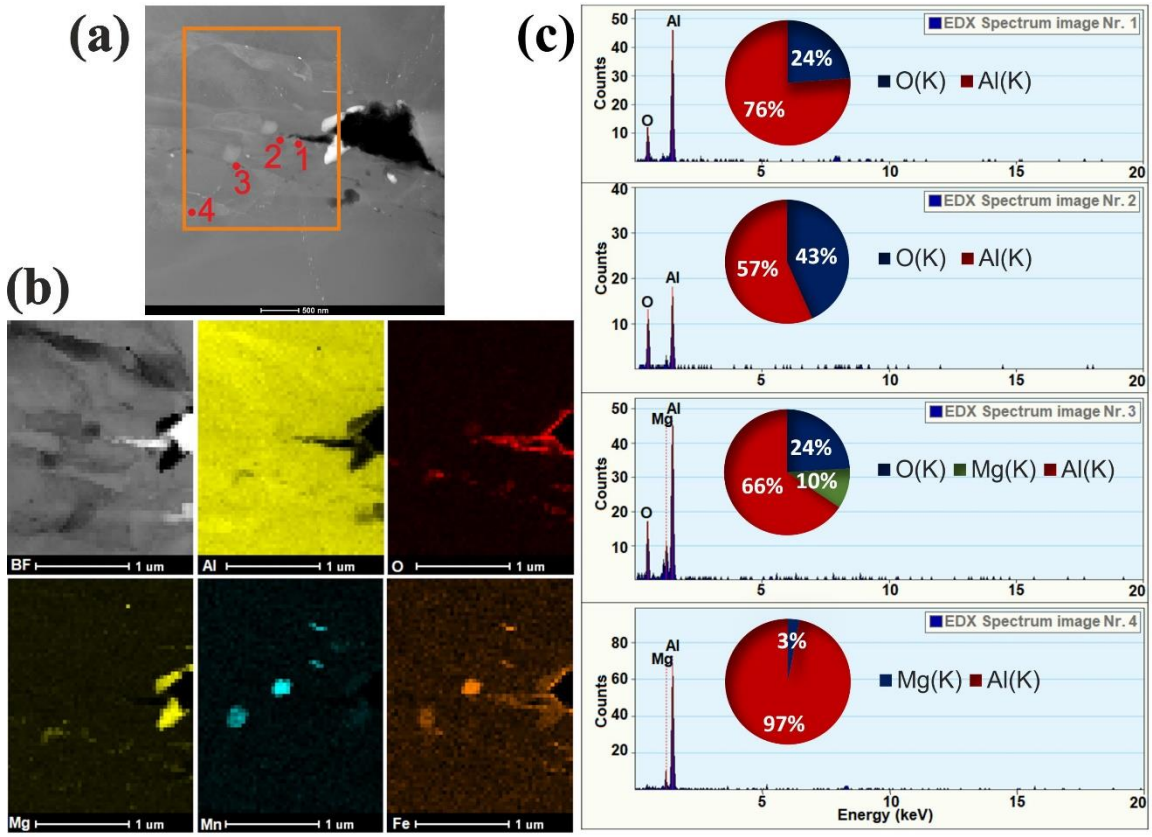

Fig. 17: Scanning transmission electron microscopy image with corresponding energy dispersive X-ray spectroscopy (STEM-EDX) elemental mapping showing the spatial distribution of the oxide and intermetallics: **(a)** High-angle annular dark-field scanning transmission electron microscope (HAADF-STEM) overview image; **(b)** Bright field scanning transmission electron microscopy image with corresponding energy dispersive X-ray spectroscopy (STEM/EDX) elemental mappings of the area marked in overview (a); **(c)** spot analysis with energy dispersive X-ray spectroscopy (EDX) spectra marked in (a).

To verify these observations, a more detailed analysis was performed using FM-KPFM which unambiguously confirmed the presence of an oxide layer nearer the micro-pits. In **Figs. 18b,c,d** a comparison of the STEM- EDX map of oxygen obtained with TEM, surface potential map and work function map is shown. In **Fig. 18a**, the topography of the electron-transparent TEM lamella analysed by FM-KPFM is presented. The work function map was estimated from the surface potential map as follows [30]:

$$\Phi_{sample} = \Phi_{probe} - e\Delta V_{CPD} \quad (2)$$

where Φ_{sample} is a work function of the sample (eV); Φ_{probe} is a work function of the probe (4.09 eV); ΔV_{CPD} is a contact potential difference between the probe (mV) and the sample extracted from the FM-KPFM results, *e*- is the charge of an electron.

Ideally, the work function obtained for aluminium varies from 4.06 to 4.41 eV, while for Al_2O_3, it can vary from 4.5 [31] to 4.7 eV [32]. **Fig. 18d** revealed different work functions in the oxygen-rich zone presented in **Fig. 18a** compared to the AA 5754 (AlMg3) base. The oxide material showed a higher work function (4.480 to 4.600 eV) than the aluminium base (4.350 to 4.460 eV). The observations from FM-KPFM were found consistent with the TEM observations.

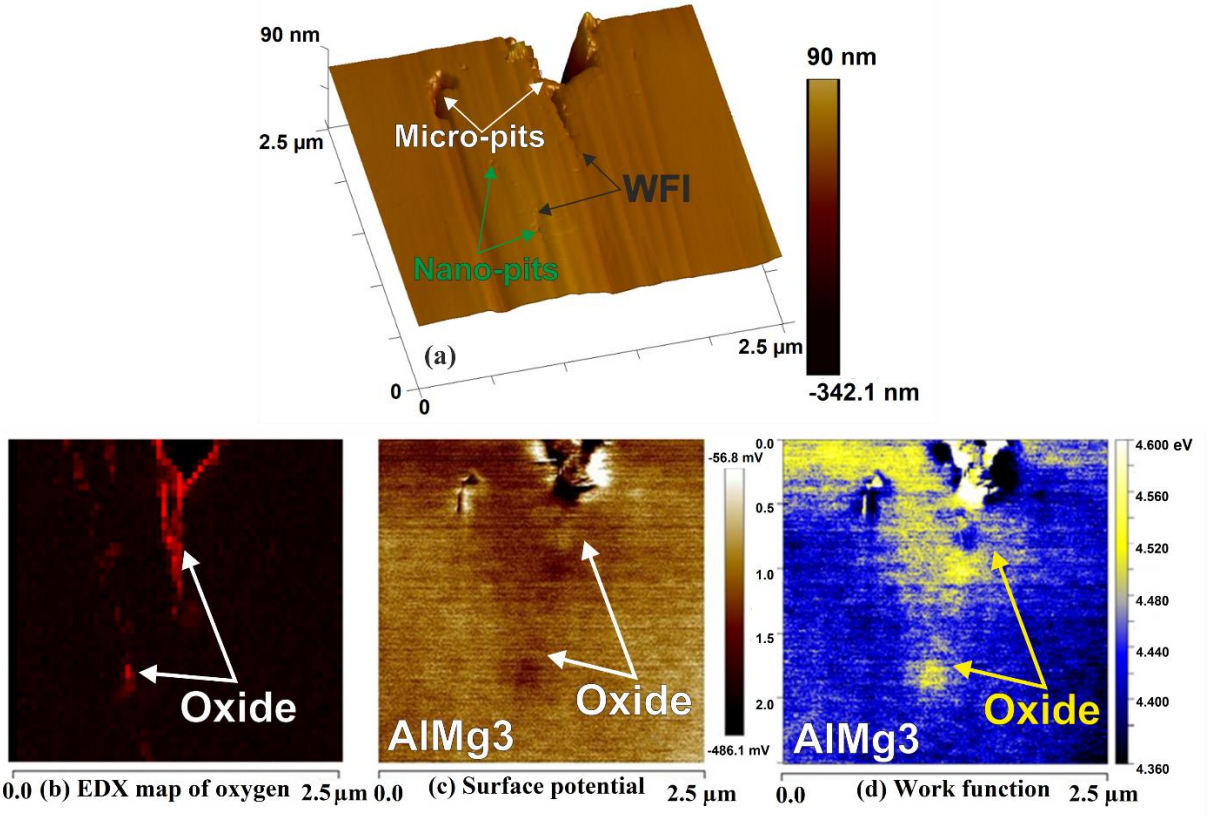

Fig. 18: (a) Topography 3D map obtained with frequency-modulated Kelvin probe force microscopy (FM-KPFM) showing the area near to the micro-pit of the sample analysed from a scanning transmission electron microscope; **(b)** energy dispersive X-ray spectroscopy map of oxygen from **Fig. 17**; **(c)** Surface potential in the same area shown in **Fig. 17a** with orange square, obtained with frequency-modulated Kelvin probe force microscopy; **(d)** work potential calculated from surface potential in (a).

WFI was observed to indeed be a complex metallurgical zone revealing the presence of multi granular phases (grain size and shapes) and different precipitate distributions. The work reported in this paper provided an improved understanding of the complex interface formed during spot welding and this has been schematically illustrated in **Fig. 19**. In **Fig. 19**, the complex metallurgy of FSSW underneath the tool was characterised in four broad regions namely (a) recrystallised stir zone (RSZ) which denotes the entire area under the influence of contact stresses during the FSSW process (b) frustrated granular refined zone (FGRZ) which

is the area separating the oxide fragments and the RSZ. In fact, one characteristic property of FGRZ is that the metallic particles separated from brittle oxides elongates, stretches and undergoes refinement leading to the formation of fibrous grains along the direction of shear load akin to the rolling process (c) diffusion resistant zone (DRZ), an area where the broken bits of metallic oxides containing nanopits were found to be heavily distributed and (d) an optional presence of dynamic precipitates (which becomes possible due to the reaction of Mg atoms with the complex interplay of dislocation climb), thus the rich presence of precipitates within the FGRZ zone is subjected to the kind of material being welded. It has been said in the past that strain hardening in the aluminium alloy used in this investigation may be a consequence of the reaction between dislocations and solute Mg atoms and precipitates. It is an aspect which would be worthy of future exploration using atomic or multiscale simulations. The FGRZ and DRZ combinedly form the WFI which causes a phase separation between two RSZ in the real-world due to the presence of oxide layer, surface roughness and imperfections in the base material prior to welding.

This study in its present form sheds light on the fact that the precipitates seen in the WFI ($Al_6(FeMn)$ and Al_3Mg_2 types) are brittle phases of AA 5754 alloy [33]. Although their distribution within the WFI was stochastic and morphology was randomised, these are directly responsible for the delamination of the FSSW joints at the interface.

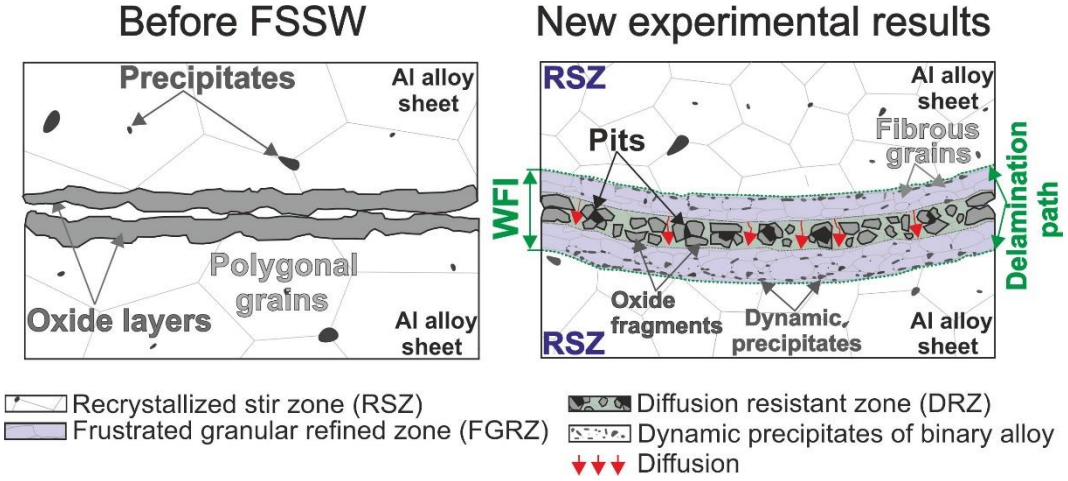

Fig. 19: Schematic illustration of the weld faying interface formed during the friction stir spot welding at low strain rate

The results from SEM and TEM analysis suggested that the smaller elongated grains are formed because of cyclic microplastic deformation of the protrusions from the rough surfaces of welded sheets at the welding interface. This additional microplastic deformation causes dislocation glide with a gradual relative rotation of adjacent subgrain [34], which can be explained by the dislocation- glide-assisted-subgrain-rotation model. The microplastic deformation of these protruded sites results in the subgrains becoming smaller elongated grains along the direction of shear load. Although the nano/micro pits were present in the middle of the WFI, it seems that delamination occurred at the periphery of WFI due to different microstructures of these two zones and by numerous Al_3Mg_2 phases at the boundary between them, serving to pave the way for the crack to nucleate. The reason why a crack did not propagate through nano and micro pits is that they were surrounded with WFI, which is a highly strain hardened zone with grain sizes at least five times smaller than grain sizes within RSZ. The Hall-Petch relationship implies that by virtue of smaller grain sizes, WFI is stronger than the RSZ [16]. Therefore, the preferred delamination site was between those zones, which were weakened by the presence of numerous precipitates.

4.0. Conclusions

Friction stir spot welding (FSSW) is an emerging solid-state joining method that is gaining increasing popularity for welding battery components, strand-terminal connectors, and terminals. One fundamental problem hitherto unaddressed in the literature about FSSW is the interfacial delamination of the weld interfaces akin to how a coating delaminates from a substrate. The indigenous experimental trials and in-depth microscopic characterisation using several microscopy techniques such as the SAM, TEM, EDX, SAM and Frequency modulated Kelvin Probe Force Microscopy together with the microhardness and small punch test revealed new insights into the complex origins of the delamination of the weld joint. The following broad conclusions were summarised based on the discussions:

(i) Two distinct weld stages, namely stick-slip and steady-state welding were observed during FSSW. During the stick-slip state, axial stress was larger than the shear stress causing 'surface friction' to dominate but as soon as the tool establishes a stable contact with the workpiece, the shear stress dominates the axially applied pressure leading to a transition of surface friction to volumetric friction.

(ii) SPT and microhardness tests revealed that the increasing rotational speed causes a transition from strain hardening of the material to thermal softening. From small punch tests, it was observed that the welds obtained at high rotational speeds underwent significant thinning of the cross-sections whereas the welds obtained at low rotation speeds become strain hardened and underwent lesser thinning. In all specimens subjected to a small punch test; a weld faying interface was visible with traces of delamination caused by the radial cracking.

(iii) The origins of the interfacial delamination of the weld joints were observed to be due to the metallurgical transformations triggered by the contact stresses leading to the formation of a complex recrystallised stir zone (RSZ) comprising of evenly distributed precipitates of $Al_6(FeMn)$ and a weld faying interface (WFI), which had five times smaller fibrous grains with a high volume of precipitates of Al_3Mg_2. Additionally, within the WFI, sites of nano- and micro-pits combined with a rich presence of Al_2O_3 and MgO were found to be present as well. The delamination occurred between RSZ and WFI due to differences in grain sizes in the two regions (WFI was a highly strain hardened zone with grains size at least 5 times smaller than grain sizes within RSZ), so Al_3Mg_2 behaved as initial fracture spots, while nano- and micro pits remain entrapped inside the hardened WFI layer.

(iv) Overall, the results showed that a convex shaped pinless tool deployed in this investigation favours the joining of multiple thin sheets at a time, which will otherwise not be possible to be achieved while using a flat tool. The stress profile created by the convex shape favours the joining process, especially if the sheets have thin geometry and the material is as soft as aluminium. Thus, the work has opened an avalanche of opportunities for joining of multiple thin alloy sheets of aluminium merely by a design-based approach to optimise the contact interface of the tool and the workpiece.

Acknowledgements

The authors are grateful to the DAAD program for financial support to perform the work. Specific thanks to the Royce PhD Equipment Access Scheme enabling access to TEM facilities

at Royce@Cambridge via UKRI Grant EP/R00661X/1. We also express thanks to the STSM support from Cost Action CA15102 (funded by H2020).SG is particularly thankful to the Research support provided by the UKRI via Grants No.: (EP/K503241/1, EP/L016567/1, EP/S013652/1, EP/T001100/1, EP/S036180/1 and EP/T024607/1). Additionally, the support received from H2020 (Cost Actions (CA18125, CA18224, CA17136 and CA16235), Royal Academy of Engineering via Grants No. IAPP18-19\295, TSP1332 and EXPP2021\1\277 and Newton Fellowship award from the Royal Society (NIF\R1\191571) is also acknowledged. This paper has also been supported by the Ministry of Education, Science and Technological Development through the project no. 451-03-68/2020-14/200156: “Innovative scientific and artistic research from the FTS activity domain”.

Data Statement

All data in the manuscript will be available through Cranfield University open repository (10.17862/cranfield.rd.12526628).

References

1. Manladan, S., et al., *A review on resistance spot welding of aluminum alloys.* The International Journal of Advanced Manufacturing Technology, 2017. **90**(1-4): p. 605-634.
2. Shirzadi, A., H. Assadi, and E. Wallach, *Interface evolution and bond strength when diffusion bonding materials with stable oxide films.* Surface and Interface Analysis: An International Journal devoted to the development and application of techniques for the analysis of surfaces, interfaces and thin films, 2001. **31**(7): p. 609-618.
3. Song, X., et al., *Effect of plunge speeds on hook geometries and mechanical properties in friction stir spot welding of A6061-T6 sheets.* The International Journal of Advanced Manufacturing Technology, 2014. **71**(9-12): p. 2003-2010.
4. Tozaki, Y., Y. Uematsu, and K. Tokaji, *Effect of tool geometry on microstructure and static strength in friction stir spot welded aluminium alloys.* International Journal of Machine Tools and Manufacture, 2007. **47**(15): p. 2230-2236.
5. Reilly, A., et al., *Modelling and visualisation of material flow in friction stir spot welding.* Journal of Materials Processing Technology, 2015. **225**: p. 473-484.
6. Assidi, M., et al., *Friction model for friction stir welding process simulation: Calibrations from welding experiments.* International Journal of Machine Tools and Manufacture, 2010. **50**(2): p. 143-155.
7. Chen, G., et al., *Effects of pin thread on the in-process material flow behavior during friction stir welding: A computational fluid dynamics study.* International Journal of Machine Tools and Manufacture, 2018. **124**: p. 12-21.
8. Kuykendall, K., T. Nelson, and C. Sorensen, *On the selection of constitutive laws used in modeling friction stir welding.* International Journal of Machine Tools and Manufacture, 2013. **74**: p. 74-85.
9. Zhao, W. and C. Wu, *Constitutive equation including acoustic stress work and plastic strain for modeling ultrasonic vibration assisted friction stir welding process.* International Journal of Machine Tools and Manufacture, 2019. **145**: p. 103434.
10. Lachowicz, D., et al., *On the influence of tooling behaviour over axial shortening mechanisms in linear friction welding of titanium alloys and modelling plasticisation effects.* International Journal of Machine Tools and Manufacture, 2021. **161**: p. 103674.
11. Sato, Y.S., et al., *Characteristics of the kissing-bond in friction stir welded Al alloy 1050.* Materials Science and Engineering: A, 2005. **405**(1-2): p. 333-338.
12. Cooper, D.R. and J.M. Allwood, *The influence of deformation conditions in solid-state aluminium welding processes on the resulting weld strength.* Journal of Materials Processing Technology, 2014. **214**(11): p. 2576-2592.

13. Sun, Y., et al., *Ultrafine grained structure and improved mechanical properties of low temperature friction stir spot welded 6061-T6 Al alloys.* Materials Characterization, 2018. **135**: p. 124-133.
14. Tier, M., et al., *The influence of refill FSSW parameters on the microstructure and shear strength of 5042 aluminium welds.* Journal of Materials Processing Technology, 2013. **213**(6): p. 997-1005.
15. Li, G., et al., *Microstructural evolution and mechanical properties of refill friction stir spot welded alclad 2A12-T4 aluminum alloy.* Journal of Materials Research and Technology, 2019. **8**(5): p. 4115-4129.
16. Sato, Y.S., et al., *Hall–Petch relationship in friction stir welds of equal channel angular-pressed aluminium alloys.* Materials Science and Engineering: A, 2003. **354**(1-2): p. 298-305.
17. Zlatanovic, D.L., et al., *An experimental study on lap joining of multiple sheets of aluminium alloy (AA 5754) using friction stir spot welding.* The International Journal of Advanced Manufacturing Technology, 2020. **107**(7): p. 3093-3107.
18. Labus Zlatanovic, D., et al., *Influence of Tool Geometry and Process Parameters on the Properties of Friction Stir Spot Welded Multiple (AA 5754 H111) Aluminium Sheets.* Materials, 2021. **14**(5).
19. Rasche, S. and M. Kuna, *Improved small punch testing and parameter identification of ductile to brittle materials.* International Journal of Pressure Vessels and Piping, 2015. **125**: p. 23-34.
20. Matocha, K., *Small-punch testing for tensile and fracture behavior: experiences and way forward*, in *Small Specimen Test Techniques: 6th Volume*. 2015, ASTM International.
21. Lakshminarayanan, A., V. Annamalai, and K. Elangovan, *Identification of optimum friction stir spot welding process parameters controlling the properties of low carbon automotive steel joints.* Journal of Materials Research and Technology, 2015. **4**(3): p. 262-272.
22. Goel, S., et al., *Designing nanoindentation simulation studies by appropriate indenter choices: Case study on single crystal tungsten.* Computational Materials Science, 2018. **152**: p. 196-210.
23. Reisgen, U., et al., *A method for evaluating dynamic viscosity of alloys during friction stir welding.* Journal of Advanced Joining Processes, 2020. **1**: p. 100002.
24. Soare, M. and W. Curtin, *Solute strengthening of both mobile and forest dislocations: The origin of dynamic strain aging in fcc metals.* Acta Materialia, 2008. **56**(15): p. 4046-4061.
25. Ozturk, F., S. Toros, and H. Pekel, *Evaluation of tensile behaviour of 5754 aluminium–magnesium alloy at cold and warm temperatures.* Materials Science and Technology, 2009. **25**(7): p. 919-924.
26. Mishra, R.S., et al., *High strain rate superplasticity in a friction stir processed 7075 Al alloy.* Scripta Materialia, 1999. **42**(2).
27. Šebek, F., et al., *Ductile fracture predictions in small punch testing of cold-rolled aluminium alloy.* Engineering Fracture Mechanics, 2019. **206**: p. 509-525.
28. Sunwoo, A., *Diffusion bonding of aluminium alloy, 8090.* Scripta Metallurgica et Materialia;(United States), 1994. **31**(4).
29. Shen, Z., et al., *Mechanical properties and failure mechanisms of friction stir spot welds of AA 6061-T4 sheets.* Materials & Design, 2013. **49**: p. 181-191.
30. Panchal, V., et al., *Standardization of surface potential measurements of graphene domains.* Scientific reports, 2013. **3**(1): p. 1-8.
31. Michaelson, H.B., *The work function of the elements and its periodicity.* Journal of Applied Physics, 1977. **48**(11): p. 4729-4733.
32. Rönnhult, T., U. Rilby, and I. Olefjord, *The surface state and weldability of aluminium alloys.* Materials Science and Engineering, 1980. **42**: p. 329-336.
33. Choi, D.-H., et al., *Behavior of β phase (Al3Mg2) in AA 5083 during friction stir welding.* Intermetallics, 2013. **35**: p. 120-127.
34. Jata, K.V. and S.L. Semiatin, *Continuous dynamic recrystallization during friction stir welding of high strength aluminum alloys.* Scripta Materialia, 2000. **43**(8): p. 743-749.